JACS
JOURNAL OF THE AMERICAN CHEMICAL SOCIETY
Article
pubs.acs.org/JACS

Reversible Transformation of Pt Nanoparticles into Single Atoms inside High-Silica Chabazite Zeolite

Manuel Moliner,[†] Jadeene E. Gabay,[‡] Chris E. Kliewer,[§] Robert T. Carr,[§] Javier Guzman,[∥] Gary L. Casty,[§] Pedro Serna,*[,§] and Avelino Corma*[,†]

[†]Instituto de Tecnología Química, Universitat Politècnica de València—Consejo Superior de Investigaciones Científicas, Avenida de los Naranjos s/n, 46022 Valencia, Spain

[‡]Astrix Technology Group, 125 Half Mile Road, Suite 200, Red Bank, New Jersey 07701, United States

[§]ExxonMobil Research and Engineering Co., Annandale, New Jersey 08801, United States

[∥]ExxonMobil Chemical Company, 4500 Bayway Drive, Baytown, Texas 77520, United States

Supporting Information

ABSTRACT: We report the encapsulation of platinum species in highly siliceous chabazite (CHA) crystallized in the presence of *N,N,N*-trimethyl-1-adamantammonium and a thiol-stabilized Pt complex. When compared to Pt/SiO_2 or Pt-containing Al-rich zeolites, the materials in this work show enhanced stability toward metal sintering in a variety of industrial conditions, including H_2, O_2, and H_2O. Remarkably, temperatures in the range 650−750 °C can be reached without significant sintering of the noble metal. Detailed structural determinations by X-ray absorption spectroscopy and aberration-corrected high-angle annular dark-field scanning transmission electron microscopy demonstrate subtle control of the supported metal structures from ∼1 nm nanoparticles to site-isolated single Pt atoms via reversible interconversion of one species into another in reducing and oxidizing atmospheres. The combined used of microscopy and spectroscopy is critical to understand these surface-mediated transformations. When tested in hydrogenation reactions, Pt/CHA converts ethylene (∼80%) but not propylene under identical conditions, in contrast to Pt/SiO_2, which converts both at similar rates. These differences are attributed to the negligible diffusivity of propylene through the small-pore zeolite and provide final evidence of the metal encapsulation.

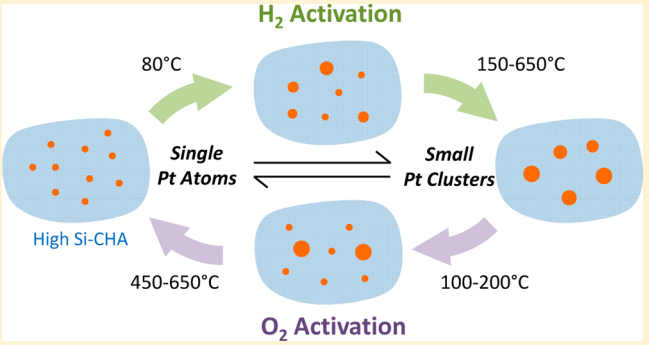

1. INTRODUCTION

Transition metals on solid supports are ubiquitous industrial catalysts for the synthesis of many chemicals.[1,2] Typically, high dispersion is desirable for better utilization of the precious metal, and most dispersed sites (i.e., clusters and single atoms) often facilitate unique catalysis that is not achieved by conventional bulk-like structures.[3,4] Unfortunately, metals tend to sinter over time in reactive environments, leading to reduction in catalyst lifetime by loss of available metal surface area and/or by annihilation of those unique metal ensembles. The concept of sinter-resistant supports has been proposed and has taken on a number of incarnations, including strong bonding between the support and the metal[5,6] and various strategies to capture metals in support cavities.[7−9] When the support is a well-structured microporous solid, such as a zeolite, opportunities arise for encapsulation of the metal nanoparticles in its channels.[10] A number of metal-containing zeolites, particularly those with medium (∼5−5.5 Å) and large pores (∼6.5−7 Å), have been prepared via post-synthetic methodologies such as metal impregnation or cation exchange.[11−13] These zeolites offer high surface areas to disperse the metal effectively, yet their relatively large pores do not confine the smallest nanoparticles and prevent their aggregation under severe reaction conditions.[14]

Trapping metals within small-pore zeolites has recently received attention as a way to enhance the sinter resistance of metals.[15] Traditional post-synthetic approaches show limitations to incorporating the metal in small-pore zeolites, in particular with metal cations of large ionic radii. One-pot methods have been proposed and must be developed to circumvent this synthetic challenge.[16,17]

Transition metal nanoparticles have been encapsulated within different low-silica small-pore zeolites, such as LTA (Linde type A),[14,16,18−22] RHO (zeolite rho),[23] and GIS (gismondine).[24] These materials are prepared without organic structure-directing agent (OSDA) at very low crystallization temperatures (∼80−100 °C); thus, only limited zeolites with very Al-rich frameworks (Si/Al ratio <3) have been achieved. While these results are interesting, low-silica zeolites suffer from

Received: September 28, 2016
Published: November 9, 2016

DOI: 10.1021/jacs.6b10169
J. Am. Chem. Soc. 2016, 138, 15743−15750

low hydrothermal stability and weaker acidity than Si-rich materials, which limits their applications as catalysts. As such, the synthesis of metal nanoparticles encapsulated in high-silica small-pore zeolites would be of both fundamental and practical interest.

Zeolites with high Si/Al ratios are synthesized using OSDA molecules,[25] often at high crystallization temperatures (above 150 °C) and high pH. In these conditions, most metal precursors tend to precipitate as rather large bulk metal hydroxides when added to the synthesis media.[16] Earlier literature demonstrates that thiol compounds stabilize metal nanoparticles, which can be dispersed in an amorphous high-surface silica matrix using a one-pot synthetic approach.[26] The high thermal stability of these mercapto-based organometallic complexes has been also demonstrated under alkaline hydrothermal conditions.[17]

Among the different small-pore zeolites reported in the literature, CHA (chabazite), formed by a three-directional small-pore system containing large cavities,[27] is an attractive candidate considering its diversity in chemical compositions,[15,27−29] crystal sizes (20 nm to 3 μm),[30] and catalytic applications.[31,32]

Herein, we present the direct synthesis of a nanocrystalline (20−50 nm) high-silica CHA zeolite containing encapsulated Pt nanoparticles of ∼1 nm, using the combination of *N,N,N*-trimethyl-1-adamantammonium (TMAda) and Pt-mercapto complex as OSDA and Pt precursor, respectively. These Pt nanoparticles have remarkable stability: they maintain ∼1 nm size at 650 °C in H_2 and steam. Moreover, quantitative transient extended X-ray absorption fine structure (EXAFS) analysis demonstrates that ∼1 nm Pt nanoparticles fragment into site-isolated single Pt atoms in O_2, and very interestingly, these single Pt atoms are stable to calcination at 650 °C. The Pt nanoparticles can be re-formed in the presence of H_2, leading to a fully reversible cluster formation/fragmentation cycle that enables fine-tuning of the catalytic structures from single metal atoms to ∼1 nm. *In situ* X-ray absorption spectroscopy (XAS) and aberration-corrected high-angle annular dark-field scanning transmission electron microscopy (AC HAADF-STEM) are used to investigate dynamic changes in the metal structures during the thermal treatments. The combination of both "average" (spectroscopy) and "local" (microscopy) information is shown to be critical to properly understand these surface-mediated transformations.

2. EXPERIMENTAL SECTION

2.1. Synthesis of Metal-Containing Zeolites. *Synthesis of N,N,N-Trimethyl-1-adamantammonium.* First, 29.6 g of 1-adamantamine (Sigma-Aldrich) and 64 g of potassium carbonate (Sigma-Aldrich) were mixed with 320 mL of chloroform. Next, 75 g of methyl iodide was added dropwise while the reaction was stirred in an ice bath. The reaction was maintained during 5 days under agitation at room temperature. The mixture was filtered and washed with diethyl ether, and the resultant solid was further extracted with chloroform. The final product was *N,N,N*-trimethyl-1-adamantammonium iodide. This iodide salt was anion exchanged using an ion-exchange resin to achieve the hydroxide form.

Synthesis of Pt-Containing High-Silica CHA Materials. The conditions for the synthesis of the Pt-containing CHA materials are summarized in Table 1. The procedure followed to carry out the preparation of the Pt-containing high-silica CHA materials is exemplified for the particular synthesis of the Pt-CHA-2 material. In this case, 800 mg of sodium hydroxide (99%, Sigma-Aldrich) was dissolved in 6.9 g of water. Next, 86 mg of a 10 wt% aqueous solution of chloroplatinic acid ($H_2PtCl_6{\cdot}6H_2O$, 37.50% Pt basis, Sigma-Aldrich) and 52 mg of (3-mercaptopropyl)trimethoxysilane (TMSH, 95%, Sigma-Aldrich) were added to the above solution, and the mixture was stirred for 30 min. Afterward, 13.04 g of an aqueous solution of *N,N,N*-trimethyl-1-adamantammonium hydroxide (TMAdA, 16.2 wt%) was added, and the mixture was maintained under stirring during 15 min. At that time, 293 mg of aluminum hydroxide (58 wt%, Sigma-Aldrich) was added, and the resultant mixture was kept under stirring at 80 °C for 30 min. Finally, 3 g of colloidal silica (Ludox AS40, 40 wt%, Aldrich) was introduced in the synthesis mixture, which was maintained under stirring at 80 °C for 30 min. The final gel composition was SiO_2:0.033 Al_2O_3:0.00033 Pt:0.005 TMSH:0.2 TMAdA:0.4 NaOH:20 H_2O. The gel was transferred to an autoclave with a Teflon liner and heated at 90 °C for 7 days, and later at 160 °C for 2 days under dynamic conditions. The sample after the hydrothermal crystallization was filtered and washed with abundant distilled water and finally dried at 100 °C.

Table 1. Synthesis Conditions Selected for the Pt-Containing High-Silica CHA Materials[a]

sample	NaOH/Si	Pt/Si [wt% Pt]	TMSH/Pt
Pt-CHA-1	0.4	0.00033 [0.11]	5
Pt-CHA-2	0.4	0.00033 [0.11]	15
Pt-CHA-3	0.2	0.00033 [0.11]	15
Pt-CHA-4	0.4	0.001 [0.33]	15

[a]Si/Al = 15, TMAda/Si = 0.2, H_2O/Si = 20. The resultant gels were treated at T = 90 °C for 7 days, and later at 160 °C for 2 or 7 days under dynamic conditions.

Synthesis of Aluminum-Rich Pt-LTA Material. A Pt-containing Al-rich LTA material has been synthesized following the methodology described by Iglesia et al.,[17] under the following synthesis conditions: SiO_2:0.7 Al_2O_3:0.002 Pt:0.06 TMSH:2.2 NaOH:60 H_2O, T = 100 °C. The gel was transferred to an autoclave with a Teflon liner and heated at 100 °C for 2 days under dynamic conditions. The sample after the hydrothermal crystallization was filtered and washed with abundant distilled water, and finally dried at 100 °C. After the synthesis procedure, the obtained solid shows the crystalline structure of the LTA material.

Synthesis of Pt/SiO_2. A catalyst consisting of platinum nanoparticles supported on amorphous silica (reference material) was prepared according to the process described in the literature.[33] In this procedure, 1.784 g of tetraammine platinum hydroxide was mixed with 12.2 g of deionized water. Next, 0.6 g of arginine was added to this solution so that the arginine-to-Pt molar ratio was 8:1. The solution was added by incipient wetness onto 10.0 g of Davison silica (grade 62, 60−200 mesh, 150 Å pore diameter from Sigma-Aldrich). The sample was dried at 120 °C for 2 h. The dried sample was placed in a tube furnace with an active air flow of 300 sccm of air, with the heating rates being maintained at 3 °C/min to 400 °C and then maintaining the temperature at 400 °C for 16 h. The chemical analysis of the resultant solid by ICE-AES indicated a Pt content of 0.8 wt%.

2.2. Characterization. *Powder X-ray Diffraction (PXRD).* PXRD measurements were performed with a multisample Philips X'Pert diffractometer equipped with a graphite monochromator, operating at 45 kV and 40 mA, and using Cu Kα radiation (λ = 0.1542 nm).

Chemical Analyses. The chemical analyses were carried out in a Varian 715-ES ICP optical emission spectrometer, after solid dissolution in HNO_3/HCl/HF aqueous solution.

Electron Microscopy. The morphology of the samples was studied by scanning electron microscopy (SEM) using a JEOL JSM-6300 microscope and by scanning transmission electron microscopy (STEM) using a JEM 2100F microscope.

N_2 Absorption. Textural properties were obtained from the N_2 adsorption isotherm measured at 77 K, in a Micromeritics ASAP 2020 apparatus.

H_2 Chemisorption. Metal dispersions in the calcined samples have been determined by H_2 chemisorption at 313 K using the double isotherm method on a Quantachrome Autosorb-1 equipment after *in situ* reduction of the sample at 673 K for 2 h under pure hydrogen flow, assuming a H:Pt adsorption stoichiometry of 1:1.

DOI: 10.1021/jacs.6b10169
J. Am. Chem. Soc. 2016, 138, 15743−15750

XAFS Experiments. XAFS experiments were performed at beamline 9-BN at Advanced Photon Source (APS) at the Argonne National Laboratory. Data were collected in fluorescence mode using an XAFS cell that also acted as a flow reactor. The samples were scanned in the presence of flowing gases (30 sccm) at variable temperatures. The *in situ* reductions were performed with 4% H_2 (in He), whereas 20% O_2 (in He) was used for the *in situ* oxidation treatments.

The storage ring electron energy and ring currents were 7.0 GeV and 105 mA, respectively. A water-cooled Si(111) monochromator was used to scan X-ray energy from −250 to 1000 eV relative to Pt-L_3 edge (11564 eV). Each sample (∼20 mg) was pressed as a thin wafer inside an airtight EXAFS cell, using a multi-ion Ge detector to collect data in fluorescence mode. Transmission XAFS measurements were carried out simultaneously with the pure Pt metals measured in reference mode for X-ray energy calibration and data alignment. Data processing and analysis were performed using the IFEFFIT package.[34] EXAFS analysis was done model-independently, and the results were not biased in favor of any assumed model about the short-range order of elements in these samples. Specifically, multiple-edge (Pt-L_3) analysis was employed by fitting theoretical FEFF6 calculations[35] to the experimental EXAFS data in *r* space. The values of passive electron reduction factor, S_0^2, were obtained to be 0.80 by fits to their corresponding standards, and were fixed in the analysis of the Pt-CHA samples. The parameters describing electronic properties (e.g., correction to the photoelectron energy origin) and local structural environment (coordination numbers *N*, bond length *R*, and their mean-squared relative derivation σ^2) around absorbing atoms were varied during fitting. In addition, the physically reasonable constraints between the fitting parameters for the first nearest neighbor (1NN) pairs were applied.

Structure of Active Sites by Aberration-Corrected HAADF-STEM. All environmental and high resolution imaging studies were conducted using a JEOL 2200FS AC STEM/TEM FEG operated at 200 kV. The microscope's probe forming system was fitted with a CEOS GmBH hexapole corrector. Simultaneous bright field (BF) and high-angle annular dark field (HAADF) STEM images were acquired as 512×512 pixel scans at 64 ms/px using Gatan's Digital Micrograph software. Metal particle size data were measured from the digital images using Gatan's Digital Micrograph software. Particle size data was plotted using KaleidaGraph software. Environmental studies were conducted in the JEOL 2200FS STEM mode using a Protochips Atmosphere In-Situ Gas Cell System utilizing MEMS heating technology. All reactions were conducted at 1 Torr under either 5% H_2/95% Ar or 100% O_2.

2.3. Catalytic Test. In a typical experiment, 40 mg of the Pt-CHA-2 (0.21 wt% Pt) or 10 mg of the Pt/SiO_2 (0.8 wt% Pt) catalysts were mixed with 1 g of neutral silica (silica gel, Davisil grade 640, 35−60 mesh) and loaded in a conventional tubular plug-flow reactor (i.d. = 6/16 in./9.53 mm). High-purity hydrogen, ethylene, propylene, and nitrogen were used for the experiments, with flow rates regulated by standard mass flow controllers. The temperature of the catalyst bed was controlled using a three-zone vertical furnace (ATS, model 3210) with a precision of ±1 °C. Prior to the hydrogenation experiment, the catalyst was reduced *in situ* in a flow of hydrogen (50 sccm) at 400 °C for 4 h. The reactor was then cooled down to the selected reaction temperature (80 °C). With the catalyst bed at 80 ± 1 °C, the reaction mixture was flowed at atmospheric pressure: 4 sccm of alkene (ethylene or propylene), 20 sccm of H_2, and 100 sccm of N_2. The downstream reaction effluents were analyzed in a gas chromatograph (Agilent 5975B) connected in series, and equipped with a 50 m capillary column (Rt-Alumina BOND/Na_2SO_4, 0.53 mm i.d., 10 μm) and a FID detector. The conditions of the analysis were as follow: initial oven temperature = 50 °C; temperature ramp = 10 °C/min; final oven temperature = 180 °C; injector temperature = 220 °C; detector temperature = 320 °C; pressure at the head of the column = 9.7 psi. For identification purposes, the position of the various reactants and products within the gas chromatogram were compared with commercially available standards. Conversions and selectivity were calculated from the corresponding GC areas.

3. RESULTS AND DISCUSSION

3.1. Synthesis and Stability of Pt-Containing High-Silica CHA Zeolite. To accomplish efficient encapsulation of Pt inside high-silica CHA, we investigated different synthesis parameters such as NaOH/Si [0.2, 0.4], TMSH/Pt [5, 15], and Pt content [0.11 and 0.33 wt% Pt] (Table 1). Other variables where chosen according to typical conditions to obtain metal-free CHA.[27,36]

The PXRD of the resultant solids indicate the formation of pure CHA in all studied cases (Figure 1). The Pt-CHA-3

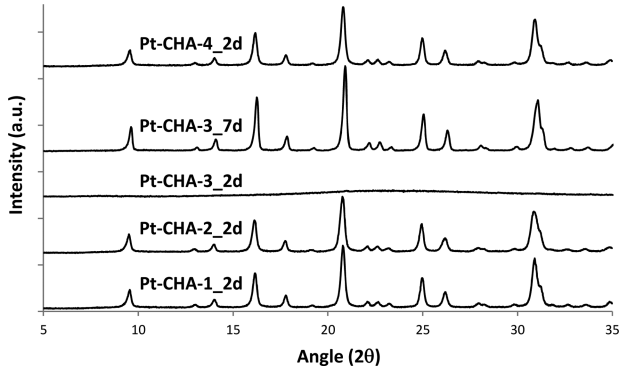

Figure 1. PXRD patterns of the as-prepared materials.

sample, synthesized with a NaOH/Si ratio of 0.2, required 7 days to crystallize and yielded crystals of ∼300 nm (Figure S1), as opposed to samples prepared at a higher NaOH/Si ratio (0.4), which fully crystallized after 2 days and formed 20−40 nm particles (Figures 1 and S2). Changes in the synthesis pH also caused changes in the solid yields, and in the molar Si/Al ratios, both lower when the pH was higher (Table 2) likely due to a fast

Table 2. Chemical Analyses on Pt-Containing High-Silica CHA Materials

sample	Si/Al	wt% Pt
Pt-CHA-1	7.8	0.23
Pt-CHA-2	8.5	0.21
Pt-CHA-3	12.2	0.17
Pt-CHA-4	8.0	0.45

nucleation of the silico-aluminate and a partial dissolution of the silica phase in the aqueous media under very alkaline conditions.[37] Nonetheless, the Si/Al ratios (>8.5) are much higher than any other reported for noble metals in small-pore zeolites.[16,18,23]

The Pt content in the samples above ranges between 0.2 and 0.45 wt%, depending on the nominal amounts in the synthesis gel (Tables 1 and 2). The dispersion of the metal phase was investigated by STEM after calcination of the materials in air at 580 °C, and after subsequent reduction in H_2 at 400 °C. The Pt-CHA-2 sample showed the smallest and narrowest distribution of Pt particles (Figure 2), with an average particle size of ∼1.4 nm (Figure 3) that is in good agreement with H_2 chemisorption data (∼1.7 nm, Table 3). This result drastically contrasts that observed for Pt-CHA-3, synthesized at a lower pH, where a major fraction of the metal is in particles >20 nm (Figure 2). We hypothesize that poor mobilization of the zeolite precursors at lower pH caused an inefficient encapsulation in Pt-CHA-3.

Small metal nanoparticles were found in materials synthesized at high pH, as in Pt-CHA-2, but using lower TMSH/Pt

DOI: 10.1021/jacs.6b10169
J. Am. Chem. Soc. 2016, 138, 15743−15750

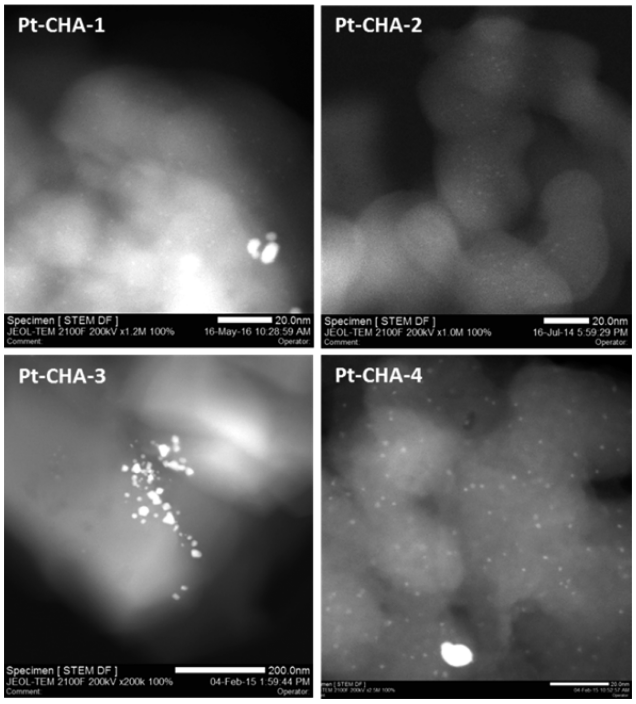

Figure 2. STEM images for the calcined Pt-containing high-silica CHA after being treated with H_2 at 400 °C.

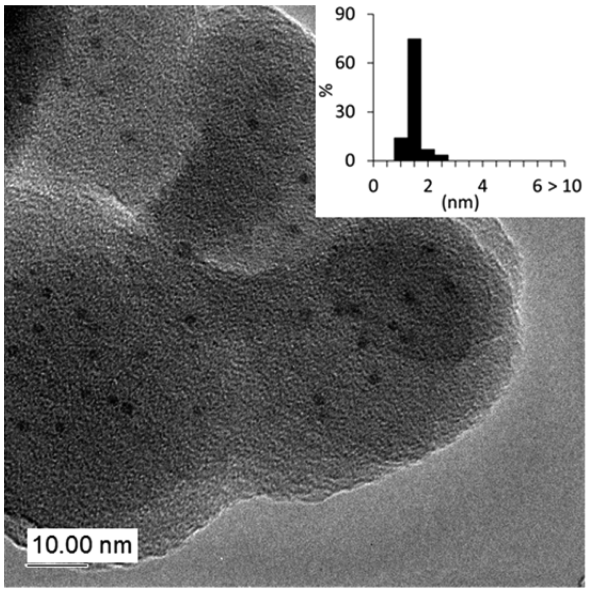

Figure 3. TEM and corresponding Pt nanoparticle size distribution histogram for sample Pt-CHA-2 after reduction in H_2 at 400 °C.

Table 3. Pt Dispersion and Average Pt Particle Size Measured by H_2 Chemisorption for Pt-CHA-2 and Pt-SiO_2 after Different Redox Treatments

sample	treatment	Pt dispersion (%)	average size (nm)
Pt-CHA-2	R400	68.0	1.7
	O650/R400	63.0	1.8
Pt-SiO_2	R400	53.0	2.1
	O650/R400	1.5	7.1

ratios (Pt-CHA-1, 5 vs 15), or higher Pt contents (Pt-CHA-4, 0.45 vs 0.21 wt%), yet together with Pt aggregates >20 nm (Figure 2). Thus, we infer that optimal results are achieved when high pH, low metal loading, and high thiol-to-platinum are used (Pt-CHA-2).

The textural properties of the calcined Pt-CHA-2 sample has been evaluated by N_2 adsorption. The N_2 adsorption isotherm clearly reveals the microporous nature of the Pt-CHA-2 (see Figure S3), whereas the obtained values for the BET and micropore areas (525 and 509 m^2/g, respectively), and micropore volume (0.25 cm^3/g) are in line with the values described in the literature for well-synthesized CHA-type materials

The stability of Pt-CHA-2 was then evaluated after high temperature oxidation/reduction treatments, to emulate conditions used to regenerate metal catalysts industrially (i.e., O_2 to remove coke deposits in hydrocarbon transformations, and H_2 to re-activate the metal function). STEM and H_2 chemisorption (Figure S4 and Table 3) demonstrate that the Pt-CHA-2 sample retains ~1.3 nm particles after a $H_2/O_2/H_2$ cycle at 400/650/400 °C for 2/4/2 h, respectively. In contrast, treatment of non-encapsulated Pt nanoparticles, supported on amorphous SiO_2, under analogous conditions resulted in massive sintering of the metal phase; particles grew from ~2 to ~7 nm, on average (Table 3). Remarkably, Pt-CHA-2 retained structural characteristics (i.e., Pt ~1.4 nm) even at harsher conditions ($H_2/O_2/H_2$ at 650/650/650 °C for 6 h per step).

We also treated the Pt-CHA-2 material with steam at high temperatures, because vapor water is common in many industrial streams and is often responsible for hydrothermal degradation of the metal and/or the zeolite framework. After subjecting Pt-CHA-2 to a severe steaming process (600 °C for 4 h), no evidence of the formation of large Pt particles was observed, and the zeolite crystallinity was retained (Figures S5 and S6). In contrast, the zeolitic structure in Pt-containing Al-rich small-pore zeolites, prepared according to literature,[17] collapsed under equivalent conditions, resulting in the formation of large Pt particles (e.g., Pt-LTA in Figures S5 and S6).

3.2. Structure of CHA-Encapsulated Platinum Species in Reducing and Oxidizing Atmospheres. We used XAS spectroscopy to gain more detailed structural information on the Pt-CHA-2 sample (Figures S7 and 4). Fitting of the EXAFS data indicate the presence of ~4 S atoms bonded to a single Pt atom in the as-made material, with a Pt−S distance of 2.32 Å (Table 4, entry 1). This is consistent with Pt-thiol complexes in square planar coordination formed by reactions of the mercaptosilane and $PtCl_6^{2-}$.[17] Calcination in air at 550 °C resulted in complete sulfur removal, and the formation of ~3 Pt−O bonds at 2.01 Å (Table 4, entry 2). EXAFS does not provide evidence of Pt−Pt bonds in either the as-made or calcined materials, consistent with the absence of Pt nanoparticles visible in STEM micrographs (Figure S2). We conclude that the calcined material consists of isolated PtO_3 units inside the zeolite. Similar species have been reported on KLTL zeolite upon calcination of $[Pt(NH_3)_4](NO_3)_2$ at moderate temperatures (250 °C), with the support acting as a macroligand that provides two O atoms to anchor the Pt.[38]

Subsequent contact with H_2 at increasing temperatures caused gradual reduction of the metal in Pt-CHA-2, as evidenced by a gradual decrease of the white line intensity in time-resolved XANES experiments (Figure 5A). Well-defined isosbestic points along the treatment suggest a rather simple stoichiometric transformation of one species into another.[39] Eventually, a steady white line intensity equal to that of a Pt foil is reached, indicating full reduction of all the metal in the sample. Figure 5B shows the

DOI: 10.1021/jacs.6b10169
J. Am. Chem. Soc. 2016, 138, 15743−15750

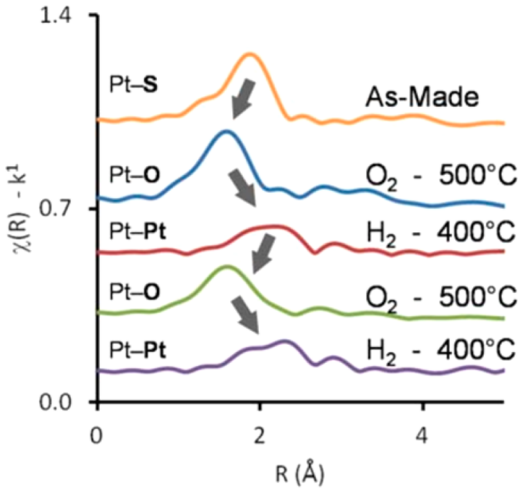

Figure 4. FT-EXAFS spectra of Pt-CHA-2 after various thermal treatments (the arrows indicate direction of the sequence and corresponding changes in structural features). First O_2 treatment performed in an oven in air (removal of organic components). Following treatments performed in a flow EXAFS cell under 30 sccm of 4% H_2 or 20% O_2.

Table 4. EXAFS Data at the Pt-L_3 Edge Characterizing the Pt-CHA-2 Sample after Various Thermal Treatments[a]

entry	contribution	N	R (Å)	$\Delta\sigma^2$ (Å^2)	ΔE_0 (eV)
1[b]	Pt–S	3.78	2.33	0.0039	7.71
2[c]	Pt–O	3.22	2.01	0.0016	12.4
3[d]	Pt–Pt	7.36	2.74	0.0580	5.83
4[e]	Pt–O	2.71	2.02	0.0034	8.36
5[f]	Pt–Pt	6.48	2.73	0.0071	5.34
	Pt–O	0.44	2.11	0.0011	11.87

[a]Notation: N, coordination number; R, distance between absorber and backscatterer atoms; $\Delta\sigma^2$, Debye–Waller factor; ΔE_0, inner potential correction. Error bounds (accuracies) characterizing the structural parameters obtained by EXAFS spectroscopy are estimated to be as follows: coordination number N, ~20%; distance R, ~0.02; Debye–Waller factor $\Delta\sigma^2$, ~20%; and inner potential correction ΔE_0, ~20%. [b]Sample as-made; spectra taken in He at 25 °C. [c]Sample in entry 1 after *ex situ* calcination in air at 550 °C for 2 h; spectra taken in air at 25 °C. [d]Sample in entry 2 after subsequent *in situ* reduction in 4% H_2 (balance, He) at 400 °C for 1 h; spectra taken in H_2 at 25 °C [e]Sample in entry 3 after subsequent *in situ* calcination in 20% O_2 (balance, He) at 500 °C for 1 h; spectra taken in air at 25 °C [f]Sample in entry 4 after subsequent *in situ* reduction in 4% H_2 (balance, He) at 500 °C for 1 h; spectra taken in air at 25 °C

degree of metal reduction at each temperature, with 0% reduction assigned to the sample before introducing H_2, when the white line intensity is highest, and 100% reduction assigned to the catalyst at the end of the treatment, when it is lowest. The data indicates that the onset temperature for reduction is <100 °C, and that full reduction is virtually accomplished at ~150 °C. With the metal fully reduced in H_2 at 400 °C, EXAFS indicates the presence of a single contribution ascribed to Pt–Pt bonds at 2.74 Å, with an average Pt–Pt coordination number of ~7 (Table 4, entry 3), consistent with particles of ~1.5 nm,[40] and thus, consistent with our STEM results (Figure 2).

We then recorded XANES spectra during a subsequent treatment in O_2 as the temperature was raised from temperature 20 to 500 °C. Figure 5C shows gradual increase of the white line intensity, corresponding to oxidation of the metal species. Again, well-defined isosbestic points are observed. Figure 5D, showing the degree of oxidation at various temperatures (based on the white line intensities), reveals that the conversion process takes place continually in the entire temperature range investigated. Steady state was only achieved at the highest temperature (500 °C). At this point, EXAFS show the lack of Pt–Pt interactions, and the re-appearance of a Pt–O contribution with a Pt–O bonding distance of 2.01 Å and a Pt–O coordination number of ~3 (Table 4, entry 4). Redispersion of the platinum nanoparticles in O_2 at 500 °C to single Pt atoms could be confirmed using AC HAADF-STEM (Figure S8). Remarkably, the cluster formation process could be reversed upon subsequent reduction of the sample in H_2 at 400 °C, with the formation of new ~1.2 nm Pt particles as demonstrated by both EXAFS (Pt–Pt coordination number ~6, Table 4, entry 5), and STEM (Figure S4).

The materials reported above allow precise reversible transformation of single Pt atoms and ~1 nm nanoparticles depending on the chemical environment and thermal conditions employed. Such a fine, cyclic control of metal species on supports is unusual, and often requires mild temperatures to avoid irreversible formation of large metal aggregates upon sintering. Rh and Ir, for example, made under inert conditions from well-define organometallic compounds such as $Rh(C_2H_4)_2(acac)$ and $Ir(C_2H_4)_2(acac)$, where acac = acetylacetonate, allow reversible transformation between small metal clusters (2–6 atoms) and single-atom metal complexes in H_2 and C_2H_4 atmospheres, respectively, at temperatures below 80 °C.[41,42] Notice that, to have single atoms, the authors always require organic ligands. On the other hand, single Pt atoms could be synthesized in a large pore zeolite (KLTL) exchanged with $[Pt(NH_3)_4](NO_3)_2$ and calcined at 250 °C.[38] This framework allows stabilization of small Pt nanoparticles (~1–1.5 nm) in H_2 provided that the temperature is <510 °C.[43] Here, by using the further constrained pore system of CHA zeolite, small Pt nanoparticles (~1–1.5 nm) and single Pt atoms could be stabilized in H_2 and O_2, respectively, at temperatures as high as 650 °C, and we demonstrate that these species can be reversibly interconverted.

Although the exact mechanism of cluster formation and fragmentation remains to be unraveled, we infer that Pt atoms hosted in different cages of the zeolite migrate in H_2 through the 8-ring windows to consolidate a final stable metal framework upon interaction. The large internal surface of the support favors the formation of the particles inside the CHA crystals, before the metal reaches the outer surface of the zeolite. To fragment the metal particles in O_2, and maintain the resultant single Pt atoms stable at very high temperatures, strong binding to the support is required, as these species are too small to be simply confined by 8-ring apertures. Most likely, the formation of site-isolated Pt atoms at this stage of the process is associated with the existence of rather well-isolated Al sites on the highly siliceous support.

3.3. Oxidative Fragmentation of Platinum Nanoparticles to Single Platinum Atoms Inside CHA. To provide better understanding of the cluster breakup process, structural determinations by EXAFS at intermediate calcination temperatures (100 and 200 °C) were performed, starting from a fully reduced Pt-CHA-2. Figure S9 and Table 5 show these EXAFS data together with the spectra of the material prior to introduction of O_2 (fully reduced), and after calcination at 500 °C (fully oxidized). The results evidence a gradual decrease

DOI: 10.1021/jacs.6b10169
J. Am. Chem. Soc. 2016, 138, 15743–15750

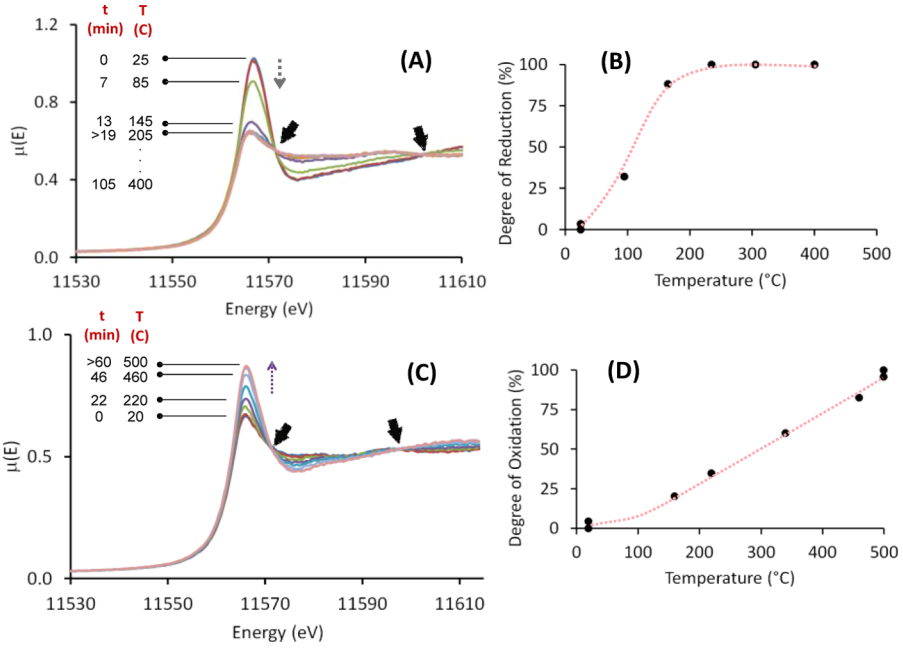

Figure 5. (A) Time-resolved XANES spectra of Pt-CHA-2 (previously calcined in air at 500 °C) in 4% H_2 as the temperature is ramped from 25 to 400 °C at 10 °C/min; (C) Time-resolved XANES spectra of Pt-CHA-2 (previous reduced in H_2 at 400 °C) in 20% O_2 as the temperature is ramped from 25 to 500 °C at 10 °C/min; (B) and (D) show the degree of reduction and oxidation, respectively, as a function of the temperature, according to white intensities (details in main text). The solid arrows point the formation of well-defined isosbestic points during the treatments.

Table 5. EXAFS Data at the Pt-L_3 Edge Characterizing the Reduced Pt-CHA-2 Sample upon Oxidation at Various Temperatures[a]

gas	T (°C)	contribution	N	R (Å)	$\Delta\sigma^2$ (Å^2)	ΔE_0 (eV)
4% H_2[b]	25	Pt−Pt	7.36	2.74	0.0580	5.83
20% O_2[c]	100	Pt−Pt	5.06	2.72	0.0087	6.84
		Pt−O	1.13	2.00	0.0039	5.48
20% O_2[c]	200	Pt−Pt	4.01	2.71	0.010	7.28
		Pt−O	1.62	1.99	0.0039	5.37
20% O_2[c]	500	Pt−Pt	–	–	–	–
		Pt−O	2.71	2.02	0.0035	8.36

[a]Notation: N, coordination number; R, distance between absorber and backscatterer atoms; $\Delta\sigma^2$, Debye−Waller factor; ΔE_0, inner potential correction. Error bounds (accuracies) characterizing the structural parameters obtained by EXAFS spectroscopy are estimated to be as follows: coordination number N, ∼20%; distance R, ∼0.02; Debye−Waller factor $\Delta\sigma^2$, ∼20%; and inner potential correction ΔE_0, ∼20%. [b]Measured after reduction of the sample in 4% H_2 at 400 °C for 1 h; spectra collected at 25 °C in H_2. [c]Measured upon attainment of a steady white line intensity in the XANES spectra (typically, after 1 h minimum in the 20% O_2 stream); spectra collected at 25 °C in O_2.

of the Pt−Pt contribution in O_2, from ∼7 to ∼5, ∼4, and ∼0 at 100, 200, and 500 °C, respectively (Table 5 and Figure S10). These changes were accompanied by gradual increase of the Pt−O coordination number from ∼0 to ∼1.1, ∼1.6, and ∼3 at 100, 200, and 500 °C, respectively (Table 5 and Figure S10). Based on this information, a decrease in the average particle size can be insinuated,[40] corresponding to ∼1.3, ∼1.0, ∼0.80, and ∼0.35 nm (diameter of a single platinum atom) at 25, 100, 200, and 500 °C, respectively.

However, EXAFS provides average structural information and is therefore insufficient to picture some details of the cluster fragmentation process.[44] Thus, we used *in situ* AC HAADF-STEM to gather local structural information. After exposure of the reduced Pt-CHA-2 material to O_2 at 500 °C inside the microscopy cell, gradual disappearance of the initial Pt nanoparticles is observed (Figure 6). Some particles remained apparently intact even at long contact times and we infer that the treatment inside the TEM cell is less efficient than that in an ideal flow reactor, where complete fragmentation of the metal particles was observed (*vide supra*). The experiment, nonetheless, reveals that the smallest Pt clusters (0.8−1 nm) are more prone to fragmentation than particles in the 1−1.5 nm size range (Figure 6C). Thus, we propose that breakup of the smallest platinum clusters at low temperature is responsible for the initial decay of the Pt−Pt coordination number during our EXAFS experiments (Table 5), with disintegration of increasingly larger crystallites as the severity of the oxidation treatment is increased.

3.4. Catalytic Activity of the CHA-Encapsulated Pt Nanoparticles. Finally, we used the hydrogenation of olefins of different sizes to demonstrate the successful encapsulation of Pt within the CHA structure. We selected ethylene (0.39 Å) and propylene (0.45 Å), because at mild temperatures the former diffuses relatively fast through the zeolite, whereas the latter diffuses very slowly.[45] As shown in Figure 7, the Pt-CHA-2 catalyst converts >80% of ethylene (to ethane) and only 2% of propylene (to propane) under identical experimental conditions. In drastic contrast, a Pt/SiO_2 sample consisting of 2 nm (average) Pt nanoparticles produces similar conversion of both olefins under the same reaction conditions (Figure 7), as one would expect in the absence of internal diffusion effects. The very low catalytic activity observed for the propylene using Pt-CHA-2 unambiguously confirms the effective encapsulation of the Pt nanoparticles within cavities of the high-silica CHA material.

DOI: 10.1021/jacs.6b10169
J. Am. Chem. Soc. 2016, 138, 15743−15750

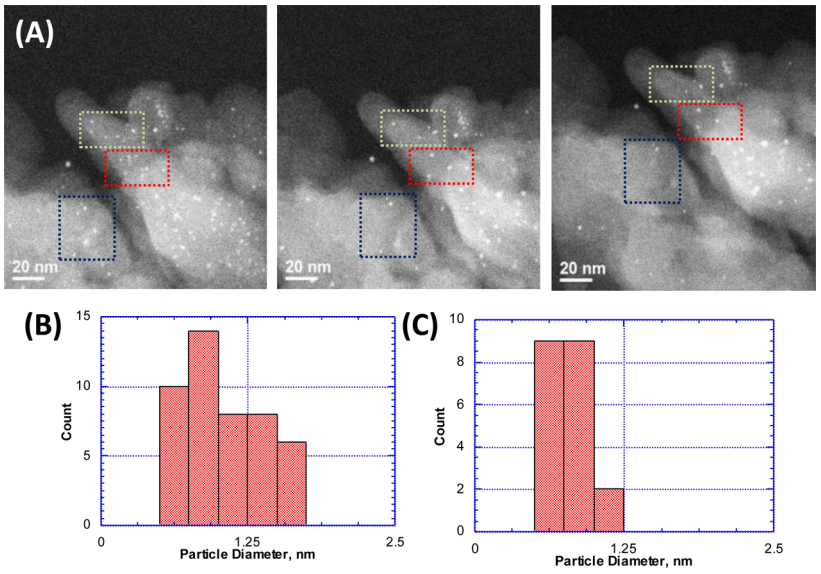

Figure 6. (A) Aberration-corrected HAADF-STEM images after contacting the reduced Pt-CHA-2 catalyst with O_2 at 500 °C for increasing times inside an environmental STEM cell (left, 0 min; middle, 10 min; right, 20 min). The areas highlighted show gradual disappearance of particles over time. (B) Particle size distribution of Pt-CHA-2 of the reduced Pt-CHA-2 (left). (C) Fraction of particles that disappears during the 20 min *in situ* O_2 treatment in the TEM cell (the biggest particles remain).

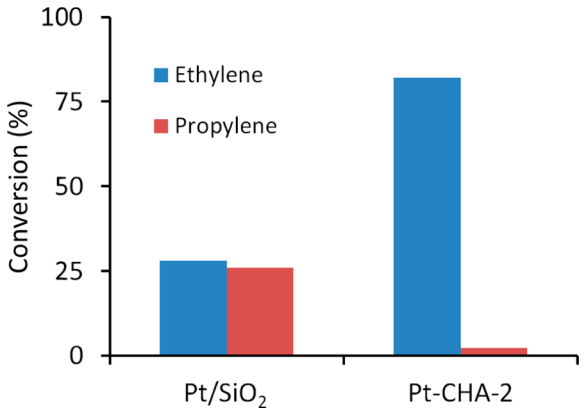

Figure 7. Hydrogenation of ethylene and propylene using 0.2 wt% Pt-CHA-2 (40 mg) and 0.8 wt% Pt/SiO_2 (10 mg) as catalysts. Reaction feed: H_2 (20 sccm), alkene (4 sccm), and N_2 (100 sccm). Reaction temperature: 80 °C. Catalysts were reduced in H_2 at 400 °C prior to reaction.

4. CONCLUSIONS

In summary, we have demonstrated the direct synthesis of nanocrystalline high-silica CHA zeolite containing encapsulated Pt species by combining the use of TMAdA and Pt-mercapto complexes as OSDA and Pt-precursors, respectively. Most importantly, it has been shown that, by controlling the activation treatment, it is possible to prepare materials in which the nature and architecture of the Pt species can be tuned reversibly, from isolated atoms to nanometric particles.

■ ASSOCIATED CONTENT

Supporting Information

The Supporting Information is available free of charge on the ACS Publications website at DOI: 10.1021/jacs.6b10169.

SEM, STEM, and HAADF-STEM images of the Pt-CHA materials, N_2 adsorption isotherm of the calcined Pt-CHA sample, XANES-EXAFS spectra of the Pt-CHA treated under different reactive atmospheres, and PXRD patterns of the Pt-containing zeolites after severe steaming treatments, including Figures S1–S10 (PDF)

■ AUTHOR INFORMATION

Corresponding Authors

*pedro.m.serna-merino@exxonmobil.com
*acorma@itq.upv.es

ORCID

Avelino Corma: 0000-0002-2232-3527

Notes

The authors declare no competing financial interest.

■ ACKNOWLEDGMENTS

This work has been supported by the European Union through the SYNCATMATCH project (Grant Agreement No. 671093) and the Spanish Government through "Severo Ochoa Program" (SEV 2012-0267) and MAT2015-71261-R. This research used beamline 9-BM of the Advanced Photon Source, a U.S. Department of Energy (DOE) Office of Science User Facility operated for the DOE Office of Science by Argonne National Laboratory under Contract No. DE-AC02-06CH11357. The Electron Microscopy Service of the UPV is acknowledged for their help in sample characterization. We thank Isabel Millet and Paul Stevens for technical assistance, and Randall Meyer, Aaron Sattler, and Dave Marler for review of the manuscript. We appreciate the support of ExxonMobil Research and Engineering for our efforts in fundamental catalytic research.

■ REFERENCES

(1) Climent, M. J.; Corma, A.; Iborra, S. *Chem. Rev.* **2011**, *111*, 1072–1133.
(2) Corma, A.; García, H. *Top. Catal.* **2008**, *48*, 8–31.
(3) Haruta, M. *Chem. Rec.* **2003**, *3*, 75–87.
(4) Oliver-Meseguer, J.; Cabrero-Antonino, J. R.; Domínguez, I.; Leyva-Pérez, A.; Corma, A. *Science* **2012**, *338*, 1452–1455.
(5) Hunt, S. T.; Milina, M.; Alba-Rubio, A. C.; Hendon, C. H.; Dumesic, J. A.; Román-Leshkov, Y. *Science* **2016**, *352*, 974–978.

DOI: 10.1021/jacs.6b10169
J. Am. Chem. Soc. 2016, 138, 15743–15750

(6) Tang, H.; Wei, J.; Liu, F.; Qiao, B.; Pan, X.; Li, L.; Liu, J.; Wang, J.; Zhang, T. *J. Am. Chem. Soc.* **2016**, *138*, 56−59.
(7) Canlas, C. P.; Lu, J.; Ray, N. A.; Grosso-Giordano, N. A.; Lee, S.; Elam, J. W.; Winans, R. E.; Van Duyne, R. P.; Stair, P. C.; Notestein, J. M. *Nat. Chem.* **2012**, *4*, 1030−1036.
(8) Lu, J.; Fu, B.; Kung, M. C.; Xiao, G.; Elam, J. W.; Kung, H. H.; Stair, P. C. *Science* **2012**, *335*, 1205−1208.
(9) Wang, G. H.; Hilgert, J.; Richter, F. H.; Wang, F.; Bongard, H. J.; Spliethoff, B.; Weidenthaler, C.; Schüth, F. *Nat. Mater.* **2014**, *13*, 293−300.
(10) Sachtler, W. M. *Acc. Chem. Res.* **1993**, *26*, 383−387.
(11) Ryoo, R.; Cho, S. J.; Pak, C.; Kim, J. G.; Ihm, S. K.; Lee, J. Y. *J. Am. Chem. Soc.* **1992**, *114*, 76−82.
(12) Guczi, L.; Kiricsi, I. *Appl. Catal., A* **1999**, *186*, 375−394.
(13) Creyghton, E. J.; van Duin, A. C. T.; Jansen, J. C.; Kooyman, P. J.; Zandbergen, H. W.; van Bekkum, H. *J. Chem. Soc., Faraday Trans.* **1996**, *92*, 4637−4642.
(14) Yang, H.; Chen, H.; Chen, J.; Omotoso, O.; Ring, Z. *J. Catal.* **2006**, *243*, 36−42.
(15) Moliner, M.; Martínez, C.; Corma, A. *Chem. Mater.* **2014**, *26*, 246−258.
(16) Zhan, B.; Iglesia, E. *Angew. Chem., Int. Ed.* **2007**, *46*, 3697−3700.
(17) Choi, M.; Wu, Z.; Iglesia, E. *J. Am. Chem. Soc.* **2010**, *132*, 9129−9137.
(18) Altwasser, S.; Gläser, R.; Weitkamp, J. *Microporous Mesoporous Mater.* **2007**, *104*, 281−288.
(19) Yang, H.; Chen, H.; Du, H.; Hawkins, R.; Craig, F.; Ring, Z.; Omotoso, O.; Munoz, V.; Mikula, R. *Microporous Mesoporous Mater.* **2009**, *117*, 33−40.
(20) Im, J.; Shin, H.; Jang, H.; Kim, H.; Choi, M. *Nat. Commun.* **2014**, *5*, 3370.
(21) Wu, Z.; Goel, S.; Choi, M.; Iglesia, E. *J. Catal.* **2014**, *311*, 458−468.
(22) Lee, S.; Lee, K.; Im, J.; Kim, H.; Choi, M. *J. Catal.* **2015**, *325*, 26−34.
(23) Chen, H.; Yang, H.; Omotoso, O.; Ding, L.; Briker, Y.; Zheng, Y.; Ring, Z. *Appl. Catal., A* **2009**, *358*, 103−109.
(24) Goel, S.; Wu, Z.; Zones, S. I.; Iglesia, E. *J. Am. Chem. Soc.* **2012**, *134*, 17688−17695.
(25) Moliner, M.; Rey, F.; Corma, A. *Angew. Chem., Int. Ed.* **2013**, *52*, 13880−13889.
(26) Budroni, G.; Corma, A. *Angew. Chem., Int. Ed.* **2006**, *45*, 3328−3331.
(27) Zones, S. I. U.S. Patent 4544538, 1985.
(28) Zones, S. I.; Hwang, S. J. *Microporous Mesoporous Mater.* **2011**, *146*, 48−56.
(29) Ashtekar, S.; Chilukuri, S. V. V; Chakrabarty, D. K. *J. Phys. Chem.* **1994**, *98*, 4878−4883.
(30) Zones, S. I.; Yuen, L.; Miller, S. J. U.S. Patent 6709644, 2004.
(31) Martinez-Franco, R.; Moliner, M.; Thogersen, J. R.; Corma, A. *ChemCatChem* **2013**, *5*, 3316−3323.
(32) Sun, Q.; Wang, N.; Guo, G.; Yu, J. *Chem. Commun.* **2015**, *51*, 16397−16400.
(33) Xu, T.; Helton, T. E.; Dakka, J. M.; Chen, T. J.; Miseo, S.; Decaul, L. C.; Lemon, E. A. World Patent WO2011/096999, 2011.
(34) Ravel, B.; Newville, M. *J. Synchrotron Radiat.* **2005**, *12*, 537−541.
(35) Zabinsky, S. I.; Rehr, J. J.; Ankudinov, A.; Albers, R. C.; Eller, M. J. *Phys. Rev. B: Condens. Matter Mater. Phys.* **1995**, *52*, 2995−3009.
(36) Martin, N.; Moliner, M.; Corma, A. *Chem. Commun.* **2015**, *51*, 9965−9968.
(37) Iler, R. K. *The Chemistry of Silica: Solubility, Polymerization, Colloid and Surface Properties and Biochemistry of Silica*; Wiley: Weinheim, 1979.
(38) Kistler, J. D.; Chotigkrai, N.; Xu, P.; Enderle, B.; Praserthdam, P.; Chen, C. Y.; Browning, N. D.; Gates, B. C. *Angew. Chem., Int. Ed.* **2014**, *53*, 8904−8907.
(39) Wang, Q.; Hanson, J. C.; Frenkel, A. I. *J. Chem. Phys.* **2008**, *129*, 234502−234507.
(40) de Graaf, J.; van Dillen, A. J.; de Jong, K. P.; Koningsberger, D. C. *J. Catal.* **2001**, *203*, 307−321.
(41) Uzun, A.; Gates, B. C. *Angew. Chem., Int. Ed.* **2008**, *47*, 9245−9248.
(42) Serna, P.; Gates, B. C. *J. Am. Chem. Soc.* **2011**, *133*, 4714−4717.
(43) Treacy, M. M. J. *Microporous Mesoporous Mater.* **1999**, *28*, 271−292.
(44) Kulkarni, A.; Lobo-Lapidus, R. J.; Gates, B. C. *Chem. Commun.* **2010**, *46*, 5997−6015.
(45) Hedin, N.; DeMartin, G. J.; Roth, W. J.; Strohmaier, K. G.; Reyes, S. C. *Microporous Mesoporous Mater.* **2008**, *109*, 327−334.

DOI: 10.1021/jacs.6b10169
J. Am. Chem. Soc. 2016, 138, 15743−15750